The Astrophysical Journal, 956:135 (7pp), 2023 October 20 https://doi.org/10.3847/1538-4357/acf717

Deep Search for Molecular Oxygen in TW Hya

Becky J. Williams[1], L. Ilsedore Cleeves[1], Christian Eistrup[1,2], and Jon P. Ramsey[1]
[1] Department of Astronomy, University of Virginia, Charlottesville, VA 22904, USA; rjw9dmj@virginia.edu
[2] Max Planck Institute for Astronomy, Königstuhl 17, D-69117 Heidelberg, Germany
Received 2023 May 17; revised 2023 August 31; accepted 2023 September 4; published 2023 October 17

Abstract

The dominant form of oxygen in cold molecular clouds is gas-phase carbon monoxide (CO) and ice-phase water (H_2O). Yet, in planet-forming disks around young stars, gas-phase CO and H_2O are less abundant relative to their interstellar medium values, and no other major oxygen-carrying molecules have been detected. Some astrochemical models predict that gas-phase molecular oxygen (O_2) should be a major carrier of volatile oxygen in disks. We report a deep search for emission from the isotopologue $^{16}O^{18}O$ ($N_J = 2_1 - 0_1$ line at 233.946 GHz) in the nearby protoplanetary disk around TW Hya. We used imaging techniques and matched filtering to search for weak emission but do not detect $^{16}O^{18}O$. Based on our results, we calculate upper limits on the gas-phase O_2 abundance in TW Hya of (6.4–70) $\times 10^{-7}$ relative to H, which is 2–3 orders of magnitude below solar oxygen abundance. We conclude that gas-phase O_2 is not a major oxygen carrier in TW Hya. Two other potential oxygen-carrying molecules, SO and SO_2, were covered in our observations, which we also do not detect. Additionally, we report a serendipitous detection of the $C^{15}N$ $N_J = 2_{5/2} - 1_{3/2}$ hyperfine transitions, $F = 3 - 2$ and $F = 2 - 1$, at 219.9 GHz, which we found via matched filtering and confirm through imaging.

Unified Astronomy Thesaurus concepts: Astrochemistry (75); Protoplanetary disks (1300)

1. Introduction

Protoplanetary disks provide a critical link in understanding the chemical evolution from the interstellar medium (ISM) to planetary systems (including our own solar system). By studying these environments, we can understand how molecular abundances change as stars, and later planets, form. Such observations are helpful to put our own solar system into context. So far, there have been about 300 unique molecules (not including isotopologues) detected in the ISM. Within protoplanetary disks, only 25 unique molecules have been detected (McGuire 2022). This low detection rate is not due to decreased chemistry in disks, but because we do not know some of the key tracers of the most abundant elements, such as oxygen.

Oxygen is the third most abundant element in the Universe, with a solar oxygen abundance of 4.9×10^{-4} relative to hydrogen (Asplund et al. 2009, 2021). The vast majority of oxygen in the Universe is incorporated into gas-phase molecules, ice-phase molecules, or refractory dust. Whittet (2010) considered the incorporation of oxygen into silicates and oxides and estimated that the amount of oxygen in dust is (0.9–1.4) $\times 10^{-4}$ relative to hydrogen in different ISM environments.

van Dishoeck et al. (2021) discuss the oxygen budget of ISM environments, assuming a total oxygen abundance of 5.8×10^{-4} relative to hydrogen (Przybilla et al. 2008). They note that about 20% of the total abundance of oxygen is unaccounted for in diffuse clouds, increasing to 50% in dense regions. Two of the most common molecules in the ISM and protoplanetary disks are carbon monoxide (CO) and water (H_2O). In warm gas in the ISM, gas-phase CO has an abundance of about 10^{-4} relative to hydrogen (Ripple et al. 2013), but is observed to be less abundant in protoplanetary disks (Dutrey et al. 1994; Ansdell et al. 2016; Long et al. 2017). Similarly, water ice has an abundance of H_2O/H_2 $\approx 10^{-4}$ in dense clouds (see van Dishoeck et al. 2013), but water vapor has been detected in low abundance in only a few disks (Du et al. 2017). It is possible that a large amount of oxygen is in frozen species, such as water ice, that are difficult to observe. Another possibility is that oxygen is in other gas-phase molecules, such as molecular oxygen (O_2).

O_2 has been observed in low abundances in two molecular clouds: O_2/H_2 $\approx (0.3–7.3) \times 10^{-6}$ in Orion (Goldsmith et al. 2011) and $O_2/H_2 \approx 5 \times 10^{-8}$ in ρ Oph A (Liseau et al. 2012). O_2 is a reactive molecule, and its most common form, $^{16}O^{16}O$, is difficult to detect due to a lack of a permanent dipole moment. The less-abundant isotopologue $^{16}O^{18}O$ does, however, have a dipole moment. Through this isotopologue, O_2 was tentatively detected in the protostellar system IRAS 16293-2422 B (Taquet et al. 2018). There have been no other reported detections of O_2 in protoplanetary disks.

Interestingly, O_2 has been detected in our own solar system in comets, which we do not expect to have undergone much chemical evolution since their formation in the pre-solar nebula. For example, O_2 was detected in the coma of comet 67P/Churyumov–Gerasimenko (67P) by the ROSINA (Balsiger et al. 2007) instrument on ESA's Rosetta spacecraft. Bieler et al. (2015) found an unexpectedly high average O_2 to water ratio of 3.80% ± 0.85%, making O_2 the fourth most abundant species in the coma. O_2 was also detected in comet 1P/Halley at an abundance of 3.7% ± 1.7% relative to water (Rubin et al. 2015). In both cases, O_2 and H_2O abundance appear to be correlated. As described in (Luspay-Kuti et al. 2018 and references therein), there have been many proposed origins for O_2 in comets, ranging from in situ processes to origins in the ISM prior to formation of the solar nebula. Recent analysis by Luspay-Kuti et al. (2022) shows that, farther from the Sun, O_2 abundance in 67P is more strongly correlated with CO and CO_2 than with H_2O. They suggest that 67P has

two reservoirs of O_2: a deep primordial nucleus of CO and CO_2 ice, and a surface layer of H_2O ice that formed later.

If O_2 in comets is not formed in situ, then it must have been present in the protoplanetary disk from whence the comet formed. This scenario is supported by chemical models that predict a large amount of oxygen is in gas-phase O_2 in the inner regions of disks. For example, O_2 ice can be produced on dust grain surfaces and under certain conditions desorbs faster than it reacts to form other molecules. Eistrup et al. (2018) predict that this process occurs in the midplane of disks, resulting in a buildup of gas-phase O_2 between the H_2O and O_2 ice lines (between 0.7 and 10 au after 8 million years). Walsh et al. (2015) meanwhile predict that gas-phase O_2 builds up in the atmosphere of T Tauri disks, produced via gas-phase neutral–neutral reactions of O + OH. They predict that O_2 may carry 50% of the total oxygen in the disk's atmosphere, and 10% when including the midplane.

In this paper, we present a deep search for $^{16}O^{18}O$ emission in the Atacama Large Millimeter/submillimeter Array (ALMA) observations of TW Hya, a well-studied T Tauri protoplanetary disk. TW Hya's relatively gas-rich disk and nearby proximity make it a good candidate for searching for faint emission. There have been many observations of gas emission lines in TW Hya, and previous observations have shown that CO gas is 1–2 orders of magnitude less abundant than in the ISM (Favre et al. 2013; Cleeves et al. 2015). Water vapor has a maximum observed abundance of $H_2O/H_2 \approx 10^{-7}$ in TW Hya (Hogerheijde et al. 2011). Evidently, gas-phase CO and H_2O do not account for the majority of oxygen in TW Hya. Could oxygen be hiding in gas-phase O_2?

2. Observations

Observations of the $^{16}O^{18}O$ $N_J = 2_1 - 0_1$ line at 233.946 GHz toward TW Hya were carried out as part of ALMA program 2019.1.01177.S (PI: Eistrup). Observations occurred on two nights in 2021, April 4 and April 6, for a combined time of 91 minutes on source. On April 4, there were 44 antennas and baselines of 15–1398 m, and on April 6, 45 antennas and baselines of 15–1263 m. J1058 + 0133 was adopted as the amplitude and bandpass calibrator, while J1037-2934 was used for phase calibration. The data were calibrated using the standard ALMA pipeline.

We searched for $^{16}O^{18}O$ emission in both the image plane and the visibility plane, as described in more detail in the following section. Subsequent imaging and analysis were carried out using the Common Astronomy Software Applications (CASA) version 6.4 (McMullin et al. 2007). Continuum emission was subtracted using the task *uvcontsub*, applying a fit order of 1 and excluding edge channels. The data were imaged using *tclean*, initially with a natural weighting scheme to improve line sensitivity. The resulting beam is 0.″59 by 0.″50 with a position angle of −88°, equivalent to a spatial resolution of 30–35 au at a distance of 60.1 pc (Bailer-Jones et al. 2018). The rms noise is 2.59 mJy beam^{-1} for a channel width of 0.235 km s^{-1}. For the matched filtering analysis, Earth's rotation was first corrected for using the CASA task *cvel*.

3. Methods

We first created a Keplerian mask (Teague 2020) to use with the CASA *tclean* task. Due to the rotation of disks, we observe some emission to be shifted to higher or lower frequencies, so certain regions of the disk will be brighter in different channels. A Keplerian mask traces this emission pattern, based on the parameters of the disk, to improve the signal to noise of the integrated intensity (e.g., Salinas et al. 2017; Teague et al. 2022). We assumed a systemic velocity of 2.86 km s^{-1} (Favre et al. 2013), distance of 60.1 pc (Bailer-Jones et al. 2018), inclination =5.°8, position angle =151°, and stellar mass = 0.81 $M_\odot$ (Teague et al. 2019). The mask was created using CO $J = 3 - 2$ emission data for TW Hya from Huang et al. (2018), and parameters optimized to fully trace the CO emission. Specifically, we set the target_res = 0.4, which convolves the mask with a circular beam of 0.″4 FWHM, and $dV0 = 500$ m s^{-1}, which affects the radially varying line width of emission. Two masks were then created for the O_2 data, one with a radius set to 100 au (convolved to 120 au), and a second with a radius set to 240 au (convolved to 260 au, covering the extent of the CO emission). Both masks were used separately in cleaning, using a 5σ threshold. The resulting image was the same in both cases because there were no values above 5σ within either mask.

The *tclean* task has several parameters that can be varied to bring out faint emission. For example, the choice of weighting scheme and uvtaper can be tuned to give a higher weighting to shorter baselines to increase sensitivity, at the expense of a lower resolution. Because we were mainly interested in looking at the disk integrated flux, we did not need the full spatial resolution of the observations. We imaged the data with several combinations of the Briggs weighting robust parameter (Briggs 1995) and uvtaper. We used channel averaging as another method of revealing faint emission. The original channel width of the data was 0.078 km s^{-1}, and we experimented with averaging two, three, and five channels together.

Matched filtering is a technique to detect weak emission in observational data (Loomis et al. 2018a). Matched filtering is applied in the visibility plane and therefore does not involve any imaging. It requires a filter that models the expected pattern of emission across velocity channels. The filter is Fourier transformed to generate a kernel that is then cross-correlated with the data. The result is an impulse response spectrum, with peaks indicating possible emission. For matched filtering, we used both Keplerian masks as filters (one with a 120 au radius, and one with a 260 au radius). It is possible that O_2 emission covers a smaller area than these radii and could be hidden in the noise. However, Keplerian masks cover less area in edge channels, so a smaller mask is below the resolution of the images.

4. Results

4.1. Imaging Results

Figure 1 shows the data imaged with natural weighting and velocity averaging to a channel size of 0.235 km s^{-1}. For all attempted combinations of imaging parameters, no significant detection was found within either choice of mask. A spectrum, calculated within 260 au, is shown in Figure 2. The average rms noise level per channel in Figure 1 is 2.59 mJy beam^{-1}. We calculated a disk integrated flux (for a velocity range of 4.69 km s^{-1}) of -11.8 ± 14.2 mJy km s^{-1} within 120 au, and 7.4 ± 18.0 mJy km s^{-1} within 260 au; i.e., at the noise level of the data, we do not detect $^{16}O^{18}O$ $N_J = 2_1 - 0_1$ emission.

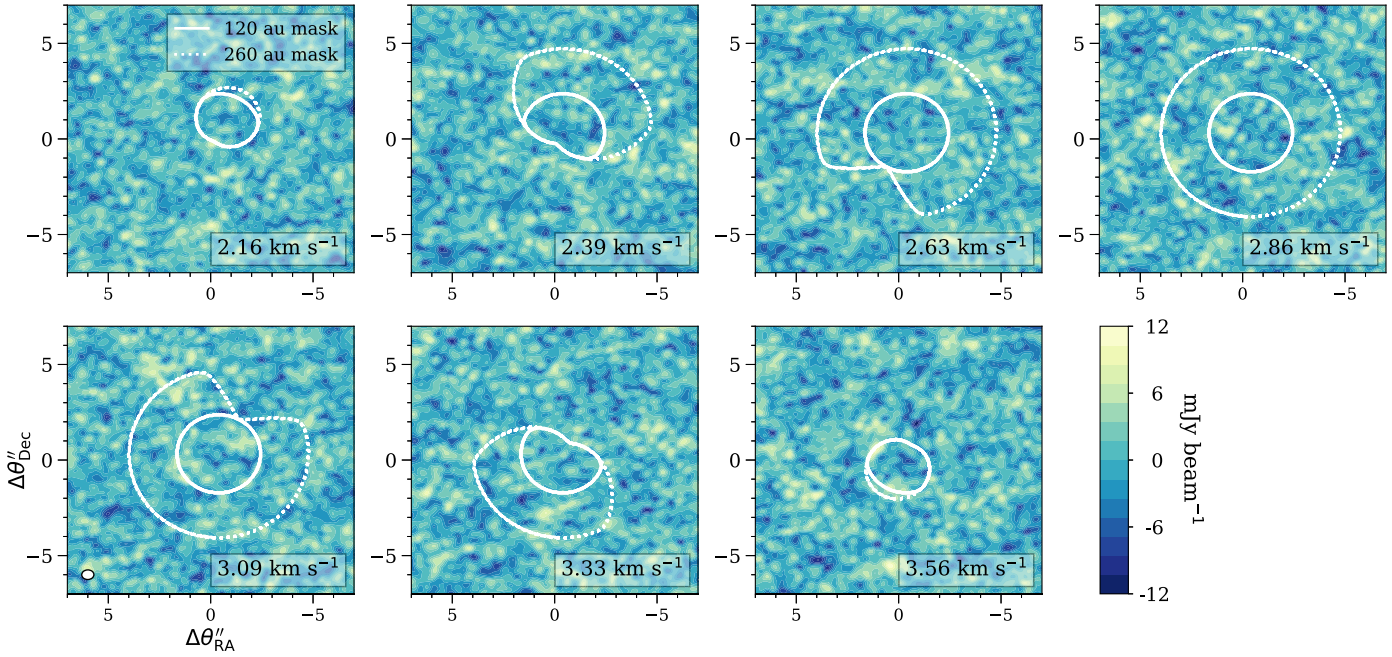

Figure 1. Channel maps of the intensity, centered on 233.946 GHz. The systemic velocity is 2.86 km s^{-1}. The two Keplerian masks are shown in white contours, and velocities are shown in the lower right of each panel. The beam size is $0\farcs59 \times 0\farcs50$ and is shown in the lower left panel.

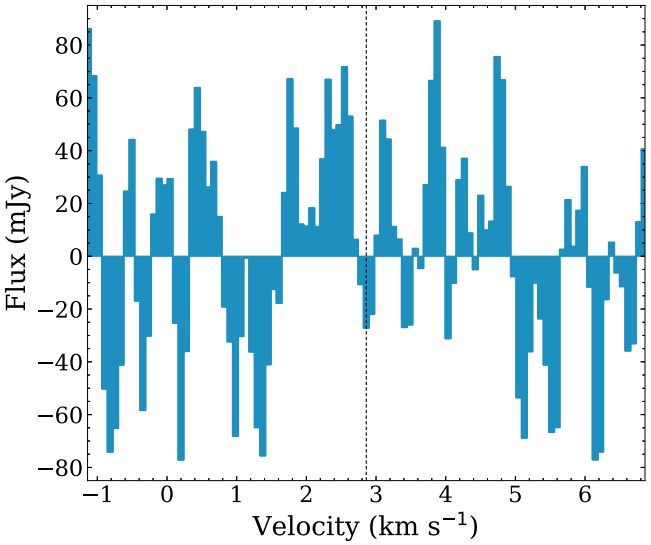

Figure 2. Spectrum of the O_2 data for TW Hya, calculated within a 260 au region. The dashed line is the systemic velocity of 2.86 km s^{-1}, centered on 233.946 GHz.

4.2. Matched Filter Results

While we cannot see emission in the image plane, if there is emission just below the noise level, matched filtering has previously been successful at finding the signatures of line emission in other sources (Loomis et al. 2020), including when using a Keplerian mask as a template (Loomis et al. 2018a). By applying the Keplerian mask as our template, we provide an expectation for where rotating gas emission should appear spatially in our data. Since we do not know the extent of the O_2, we try both the 120 and 260 au masks as templates. The results of matched filtering the data with these templates are presented in Figure 3. A 3σ response at 0 km s^{-1} would indicate emission from $^{16}O^{18}O$. Neither filter resulted in a 3σ impulse response. We can conclusively say that the $^{16}O^{18}O$ 233.946 GHz line is not detected at the sensitivity of the present measurements.

4.3. O_2 Upper Limits

How much oxygen could be hiding within our upper limit on $^{16}O^{18}O$ emission? To estimate the total number of O_2 atoms from a single line, we explore a range of temperatures and assume its emission is in local thermodynamic equilibrium. Using the image-plane disk integrated flux limits from Section 4.1, we calculate the 1σ upper limit on the maximum number of O_2 molecules that could be present in TW Hya, using the following adapted from Bergin et al. (2013):

$$F_l = \frac{\mathcal{N}_{^{16}O^{18}O} A_{20} h\nu f_u}{4\pi D^2}. \quad (1)$$

F_l is the 1σ flux calculated from our images, $\mathcal{N}_{^{16}O^{18}O}$ is the number of $^{16}O^{18}O$ molecules, $A_{20} = 1.33 \times 10^{-8}$ s^{-1} is the Einstein A coefficient of the $N_J = 2_1 - 0_1$ transition (Marechal et al. 1997), $\nu = 233.94618$ GHz is the frequency of the $N_J = 2_1 - 0_1$ transition, and $D = 60.1$ pc is the distance to TW Hya (Bailer-Jones et al. 2018). The fraction of molecules in the upper state is given by $f_u = 3.0\exp(-11.23\ \mathrm{K}\ /T)/Q(T)$, where 3 is the upper state degeneracy, 11.23 K is the upper state energy (Marechal et al. 1997), $T_{\rm gas}$ is the gas temperature, and $Q(T)$ is the partition function from the JPL spectral line catalog (Amano & Hirota 1974; Steinbach & Gordy 1975; Crownover et al. 1990; Mizushima & Yamamoto 1991; Pickett et al. 1998). These partition functions are given for temperatures ranging from 9.4 to 300.0 K, so this is the temperature range we use in our calculations. To get an upper limit on the total number of $^{16}O^{16}O$ molecules, we assumed a $^{16}O^{16}O/^{16}O^{18}O$ ratio of 280 (Wilson & Rood 1994; Taquet et al. 2018). We obtained an upper limit of $(1.1\text{–}10.4) \times 10^{49}$ O_2 molecules within 120 au,

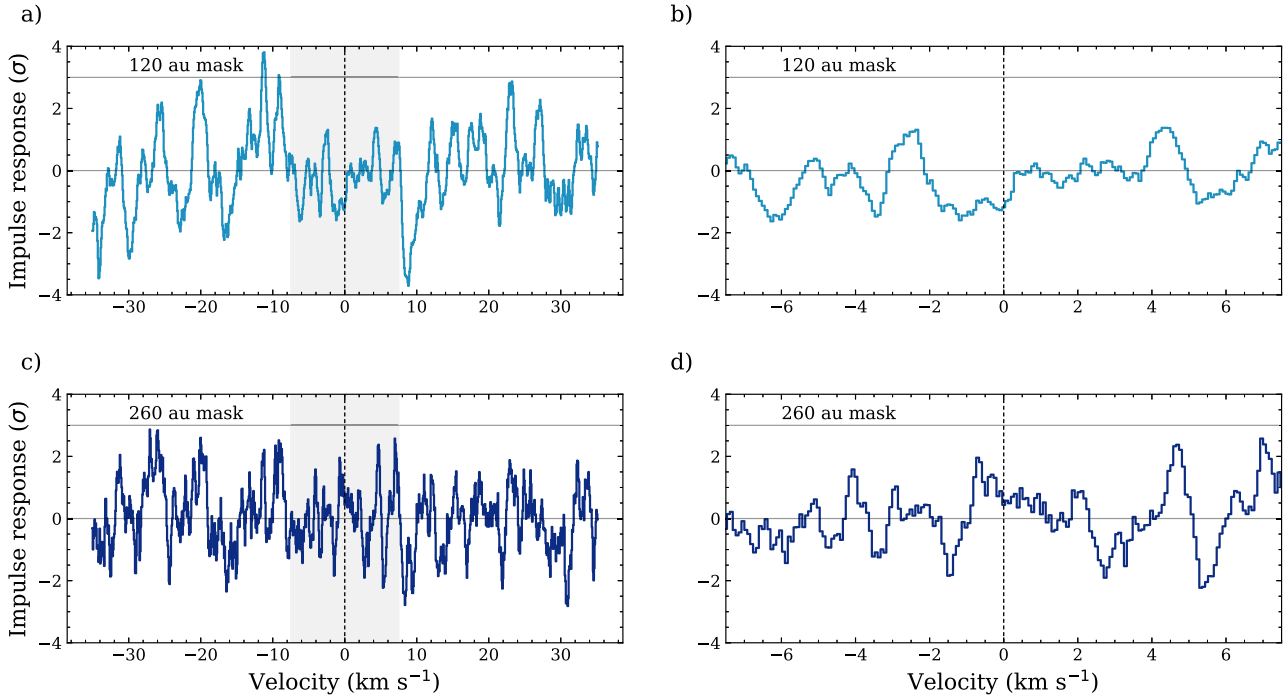

Figure 3. Matched filtering response for the $^{16}O^{18}O$ data, with impulse response on the *y*-axis and velocity on the *x*-axis. The 233.946 GHz transition is centered at 0 km s^{-1} and is denoted by the vertical dashed line. The two horizontal lines are at 0σ and 3σ. The gray region in the left plots is the range of velocities covered in the right plots. (a) 120 au filter, covering all channels. (b) Zoom-in of the shaded region in panel (a). (c) 260 au filter, covering all channels. (d) Zoom-in of the shaded region in panel (c).

and $(1.4–13.2) \times 10^{49}$ molecules within 260 au, for a temperature range of 9.4–300.0 K.

To give our result context, we also estimate the disk-averaged abundance of O_2 relative to hydrogen. To estimate the total hydrogen mass in the disk, we adopt the disk mass reported in Calahan et al. (2021), but we note that there are a wide range of mass values for the TW Hya disk in the literature (see Miotello et al. 2023). We adopt the Calahan et al. (2021) value of 2.5×10^{-2} $M_\odot$ since it uses the HD line and multiple CO isotopologues to constrain the temperature structure. Assuming a molecular mass per hydrogen molecule of 2.8 (Kauffmann et al. 2008), this equates to 2.1×10^{55} hydrogen atoms in the whole disk. Within 120 au, we use the surface density profile from Calahan et al. (2021) to calculate a disk mass of 1.8×10^{-2} $M_\odot$, which equates to 1.5×10^{55} hydrogen atoms. Using these values, we estimate an O_2/H abundance of $(7.2–70) \times 10^{-7}$ within 120 au, and $(6.4 - 62) \times 10^{-7}$ within 260 au, for temperatures ranging from 9.4 to 300.0 K. We will return to the implications of these results in Section 5.

4.4. Constraints from Serendipitous Molecular Lines

The SO $N_J = 5_6 - 4_5$ and SO_2 $N_J = 4_{(2,2)} - 3_{(1,3)}$ lines at 219.949 GHz and 235.152 GHz, respectively, were also included in the observational setup. Given that these molecules might be prominent oxygen carriers, we searched for emission from these lines using similar techniques as for $^{16}O^{18}O$. Neither line was detected above 3σ with imaging or matched filtering (see Figure 6 in the Appendix). The disk integrated flux for the SO line is -0.05 ± 12.5 mJy km s^{-1} within 120 au and -21.4 ± 21.2 mJy km s^{-1} within 260 au (covering a range of 4.99 km s^{-1}). For SO_2, the flux is 24.4 ± 14.8 mJy km s^{-1} within 120 au and 34.3 ± 24.5 mJy km s^{-1} within 260 au (covering a range of 4.67 km s^{-1}). We modified Equation (1) for SO and SO_2, using values from LAMDA (Schöier et al. 2005) and CDMS (Müller et al. 2001), and partition functions from the JPL spectral line catalog (Amano & Hirota 1974; Clark & De Lucia 1976; Helminger & De Lucia 1985; Lovas 1985; Alekseev et al. 1996; Pickett et al. 1998). We calculate a 1σ upper limit of SO/H = $(2.4–10) \times 10^{-13}$ within 120 au and $(2.9–12) \times 10^{-13}$ within 260 au, and SO_2/H = $(7.9–197) \times 10^{-13}$ within 120 au and $(9.1–229) \times 10^{-13}$ within 260 au, for a temperature range of 9.4 K to 300.0 K.

We also report a serendipitous detection of the $C^{15}N$ $N_J = 2_{5/2} - 1_{3/2}$ hyperfine transitions, $F = 2 - 1$ and $F = 3 - 2$, at 219.93404 GHz and 219.93482 GHz, respectively. Using matched filtering with the 120 au Keplerian mask, we obtained a 7σ filter response. The emission is visible in images (not shown), with an integrated flux of 113.5 ± 17.0 mJy km s^{-1} for a range of 2.33 km s^{-1}, calculated within a 200 au circular region covering visible emission. For these images, we used Briggs weighting (robust = 2) and a uvtaper of $0\farcs3$. The flux per channel is shown in Figure 4. $C^{15}N$ has previously been detected in TW Hya through its $N = 3 - 2$ transition (Hily-Blant et al. 2017). They used two methods to calculate an integrated flux of 150 ± 20 mJy km s^{-1} and 160 ± 13 mJy km s^{-1}, the first of which is consistent with our value.

5. Discussion

How does O_2 stack up compared to other known oxygen carriers? Figure 5 shows our upper limits on O_2 abundance as a function of temperature, compared to the solar oxygen abundance and known abundances of other major oxygen-carrying species in the ISM and in TW Hya. Since CO and H_2O each contain one oxygen atom, their abundances relative to hydrogen can be directly compared to the solar oxygen

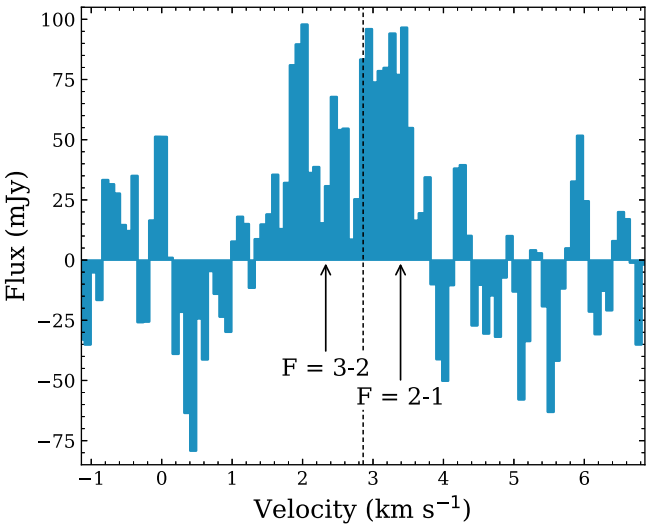

Figure 4. Spectrum of the $C^{15}N$ detection in TW Hya, calculated within a 200 au circular region. The two transitions are $N = 2 - 1$, $J = 5/2 - 3/2$ transitions, $F = 3 - 2$ and $F = 2 - 1$. The systemic velocity of 2.86 km s^{-1}, centered on the average of the two emission frequencies, is marked with the dashed line.

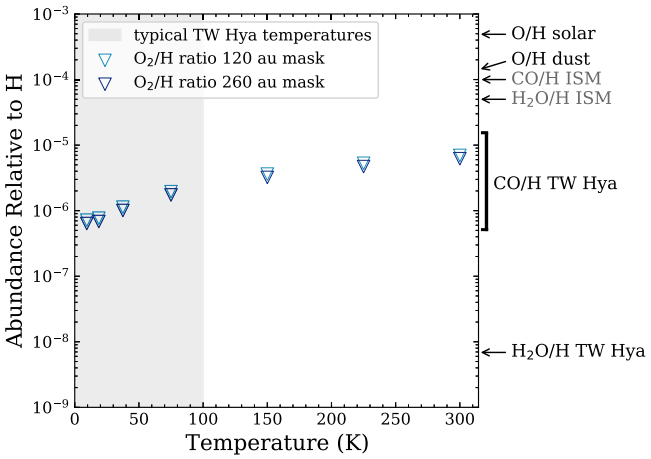

Figure 5. Upper limits on O_2 in TW Hya as a function of temperature. The shaded region shows typical temperatures in TW Hya (see Bergin & Cleeves 2018), the light blue and dark blue open triangles show the upper limits on O_2 abundance within 120 au and 260 au, respectively. Values for solar oxygen abundance (Asplund et al. 2009) and other known oxygen-carrying species are shown along the right axis. For dust, we assumed a value of 1.4×10^{-4} from Whittet (2010). From top to bottom, the remaining values used are from Ripple et al. (2013), van Dishoeck et al. (2013), Favre et al. (2013), and Zhang et al. (2013).

abundance (e.g., if all oxygen were in CO, then the CO/H abundance would equal the O/H value). O_2, on the other hand, contains two oxygen atoms, so should be multiplied by two to compare with the solar oxygen abundance.

In TW Hya, both CO gas and H_2O gas are several orders of magnitude below solar oxygen abundance; neither molecule is a major reservoir of oxygen. Our upper limit shows that gas-phase O_2 is also not a major carrier of oxygen. Other oxygen-carrying molecules that have been detected in TW Hya include HCO^+ (van Dishoeck et al. 2003), H_2CO (Öberg et al. 2017), CH_3OH (Walsh et al. 2016), and HCOOH (Favre et al. 2018), but these molecules were all detected at too low an abundance to complete the oxygen budget relative to solar values. The majority of oxygen in TW Hya has not been detected, leading to several possibilities, which we discuss further.

Our upper limits on gas-phase O_2 are not constraining enough to rule out protoplanetary disks as the origin of O_2 in comets, as water vapor in TW Hya is detected in low abundance (Zhang et al. 2013). Comets 67P and 1P/Halley were observed to have high O_2/H_2O ratios of about 0.04 (Bieler et al. 2015; Rubin et al. 2015), whereas our upper limits on gas-phase O_2 are about 2 orders of magnitude more abundant than detected water vapor in TW Hya (see Figure 5).

One possibility for the low detections of gas-phase oxygen carriers is that oxygen is frozen out, so it cannot be detected easily. Due to the low temperatures of disks, we expect many molecules (like H_2O) to exist mostly in the ice-phase, but several processes can return molecules to the gas phase throughout the entire disk. Photodesorption occurs when ultraviolet photons strike a molecule on the surface of a grain, causing the molecule to break off from the grain. It depends on the photon flux, as well as the binding energy of the molecule. Öberg et al. (2009) studied the photodesorption yield of H_2O and found that the main products are H_2O and OH. They also found that at high temperatures (100 K), up to 20% of the ice desorbs as O_2. Du et al. (2017) searched for cold water vapor in 13 protoplanetary disks, only detecting it in low abundance in two disks, and in the stacked spectrum of four other disks. They model the disk chemistry and find that, to match observations, the abundance of gas-phase oxygen must be reduced by a factor of 100 or more. They propose that oxygen (in the form of H_2O and CO) freezes onto dust grains, which then settles to the midplane (Hogerheijde et al. 2011; Bergin et al. 2016). This process primarily occurs in the outer disk; in the inner disk (within 15 au), temperatures are higher and frozen molecules may return to the gas phase. Grain size may also play a role in molecular abundances. Eistrup et al. (2022) modeled disk chemistry, taking into account grain size. They found that larger grain sizes result in a lower gas-phase O_2 abundance and a higher H_2O ice abundance, relative to the abundances produced using a fiducial 0.1 μm grain size. As grain size increases, the surface area decreases, which decreases the number of grain surface-reactions and gas-grain interactions that can occur.

Another possibility is that there is a large amount of oxygen in gas-phase molecules that we have not yet observed. Overall, the most abundant molecules detected in comets are H_2O, CO_2, and CO (Rubin et al. 2020). As discussed already, H_2O and CO have been detected in disks in low abundance. Models by Eistrup et al. (2018) predict CO_2/H abundances of up to $\approx 10^{-4}$ in disks. CO_2 gas is difficult to observe in disks because, like O_2, it is symmetric and lacks a permanent dipole moment. CO_2 has been detected in the disk within 3 au of AA Tauri (Carr & Najita 2008), using Spitzer Space Telescope observations in the mid-infrared. JWST, however, can detect ice absorption features in the infrared, including CO_2 and H_2O ices, and is already providing insight into oxygen-carrying molecules in disks (e.g., Yang et al. 2022; Grant et al. 2023; McClure et al. 2023).

6. Conclusions

We searched for but did not detect emission from gas-phase $^{16}O^{18}O$ in the protoplanetary disk around TW Hya. We used

various imaging techniques along with matched filtering, and used our results to determine an upper limit on gas-phase O_2 in TW Hya.

1. The isotopologue $^{16}O^{18}O$ was not detected in TW Hya, leading to an upper limit on the abundance of O_2 of $(7.2–70) \times 10^{-7}$ relative to H if the emission is contained within 120 au. For the whole disk, the upper limit is $(6.4–62) \times 10^{-7}$. This limit is 2–3 orders of magnitude lower than the solar oxygen abundance, so gas-phase O_2 is not a major reservoir for oxygen in TW Hya. Taking into account other existing molecular detections in TW Hya, the main oxygen carrier(s) remain undetected.
2. We place sensitive upper limits on the SO and SO_2 lines at 219.949 GHz and 235.152 GHz, respectively. We calculated an upper limit of $SO/H = (2.4 - 10) \times 10^{-13}$ within 120 au and $(2.9–12) \times 10^{-13}$ within 260 au, and of $SO_2/H = (7.9 - 197) \times 10^{-13}$ within 120 au and $(9.1–229) \times 10^{-13}$ within 260 au. These results suggest oxygen is not bound up with sulfur either.
3. We detect the isotopologue $C^{15}N$ at the 7σ level using matched filtering, and calculate an integrated flux of 113.5 ± 17.0 mJy km s^{-1}.

It is difficult to determine the main reservoir of oxygen in disks because of the many solid and gaseous forms oxygen may take (e.g., frozen H_2O, CO, CO_2; gas-phase O_2, CO_2). More observations of disks are necessary to search for this missing reservoir. Focusing on TW Hya, future searches for other gas-phase molecules, such as isotopologues of CO_2, would provide more insight on oxygen. Alternatively, searches for gas-phase $^{16}O^{18}O$ in other disks, could prove interesting. Observations of ices, especially with JWST, will also be helpful.

Acknowledgments

B.J.W. acknowledges support from the Virginia Initiative on Cosmic Origins (VICO). L.I.C. acknowledges support from the David and Lucile Packard Foundation, Research Corporation for Science Advancement Cottrell Fellowship, NASA ATP 80NSSC20K0529, NSF grant No. AST-2205698, and SOFIA Award 09-0183. C.E. acknowledges support from VICO. J.P.R. acknowledges support from the NASA Astrophysics Theory Program under grant No. 80NSSC20K0533, from the National Science Foundation (NSF) under grant Nos. AST-1910106 and AST-1910675, and from the Virginia Initiative on Cosmic Origins. This paper makes use of the following ALMA data: ADS/JAO.ALMA#2019.1.01177.S. ALMA is a partnership of ESO (representing its member states), NSF (USA) and NINS (Japan), together with NRC (Canada), MOST and ASIAA (Taiwan), and KASI (Republic of Korea), in cooperation with the Republic of Chile. The Joint ALMA Observatory is operated by ESO, AUI/NRAO, and NAOJ. All authors are grateful for support of the National Radio Astronomy Observatory (NRAO). NRAO is a facility of the National Science Foundation operated under cooperative agreement by Associated Universities, Inc.

Facility: ALMA

Software: Astropy (Astropy Collaboration et al. 2013), CASA (McMullin et al. 2007), Keplerian Mask (Teague 2020), VISIBLE (Loomis et al. 2018b).

Appendix
Matched Filter Results: Other Transitions

The matched filtering response for the data containing the SO_2 and SO transitions is shown in Figure 6. In both cases, the 120 au filter was used, and neither SO_2 nor SO were detected at the 3σ level or above. The 7σ peak at about 20 km s^{-1} in the SO spectrum is the $C^{15}N$ detection.

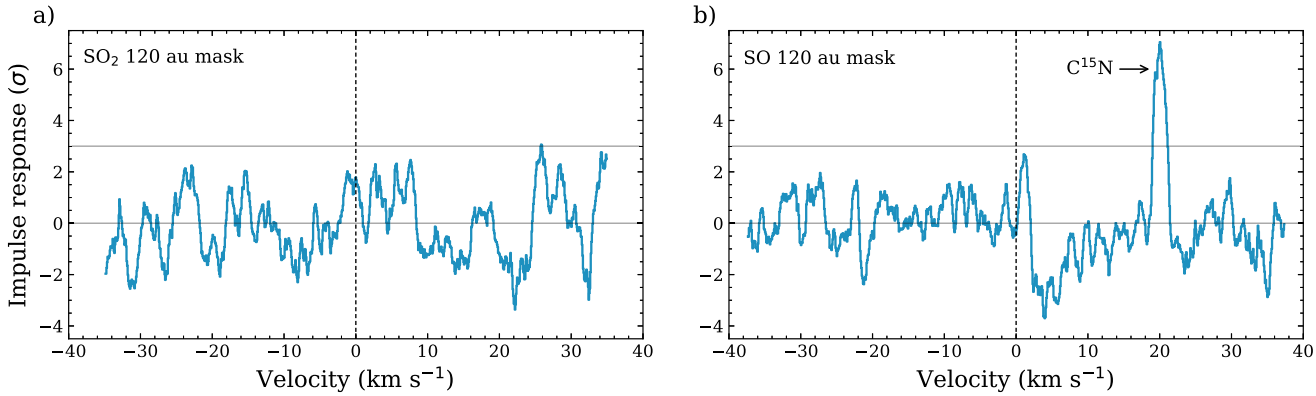

Figure 6. Matched filtering response for the data containing the SO_2 and SO transitions, with impulse response on the *y*-axis and velocity on the *x*-axis. The two horizontal lines are at 0σ and 3σ. (a) SO_2 transition, centered at 235.152 GHz (b) SO transition, centered at 219.949 GHz. The 7σ peak is the $C^{15}N$ detection.

ORCID iDs

Becky J. Williams https://orcid.org/0000-0002-1548-6811
L. Ilsedore Cleeves https://orcid.org/0000-0003-2076-8001
Christian Eistrup https://orcid.org/0000-0002-8743-1318
Jon P. Ramsey https://orcid.org/0000-0002-3835-3990

References

Alekseev, E. A., Dyubko, S. F., Ilyushin, V. V., & Podnos, S. V. 1996, JMoSp, 176, 316
Amano, T., & Hirota, E. 1974, JMoSp, 53, 346
Ansdell, M., Williams, J. P., van der Marel, N., et al. 2016, ApJ, 828, 46
Asplund, M., Amarsi, A. M., & Grevesse, N. 2021, A&A, 653, A141
Asplund, M., Grevesse, N., Sauval, A. J., & Scott, P. 2009, ARA&A, 47, 481
Astropy Collaboration, Robitaille, T. P., Tollerud, E. J., et al. 2013, A&A, 558, A33
Bailer-Jones, C. A. L., Rybizki, J., Fouesneau, M., Mantelet, G., & Andrae, R. 2018, AJ, 156, 58
Balsiger, H., Altwegg, K., Bochsler, P., et al. 2007, SSRv, 128, 745
Bergin, E. A., & Cleeves, L. I. 2018, in Handbook of Exoplanets, ed. H. J. Deeg & J. A. Belmonte (Cham: Springer), 137
Bergin, E. A., Cleeves, L. I., Gorti, U., et al. 2013, Natur, 493, 644
Bergin, E. A., Du, F., Cleeves, L. I., et al. 2016, ApJ, 831, 101
Bieler, A., Altwegg, K., Balsiger, H., et al. 2015, Natur, 526, 678
Briggs, D. S. 1995, AAS Meeting, 187, 112.02
Calahan, J. K., Bergin, E., Zhang, K., et al. 2021, ApJ, 908, 8
Carr, J. S., & Najita, J. R. 2008, Sci, 319, 1504
Clark, W. W., & De Lucia, F. C. 1976, JMoSp, 60, 332
Cleeves, L. I., Bergin, E. A., Qi, C., Adams, F. C., & Öberg, K. I. 2015, ApJ, 799, 204
Crownover, R. L., De Lucia, F. C., & Herbst, E. 1990, ApJL, 349, L29
Du, F., Bergin, E. A., Hogerheijde, M., et al. 2017, ApJ, 842, 98
Dutrey, A., Guilloteau, S., & Simon, M. 1994, A&A, 286, 149
Eistrup, C., Cleeves, L. I., & Krijt, S. 2022, A&A, 667, A121
Eistrup, C., Walsh, C., & van Dishoeck, E. F. 2018, A&A, 613, A14
Favre, C., Cleeves, L. I., Bergin, E. A., Qi, C., & Blake, G. A. 2013, ApJL, 776, L38
Favre, C., Fedele, D., Semenov, D., et al. 2018, ApJL, 862, L2
Goldsmith, P. F., Liseau, R., Bell, T. A., et al. 2011, ApJ, 737, 96
Grant, S. L., van Dishoeck, E. F., Tabone, B., et al. 2023, ApJL, 947, L6
Helminger, P. A., & De Lucia, F. C. 1985, JMoSp, 111, 66
Hily-Blant, P., Magalhaes, V., Kastner, J., et al. 2017, A&A, 603, L6
Hogerheijde, M. R., Bergin, E. A., Brinch, C., et al. 2011, Sci, 334, 338
Huang, J., Andrews, S. M., Cleeves, L. I., et al. 2018, ApJ, 852, 122
Kauffmann, J., Bertoldi, F., Bourke, T. L., Evans, N. J., & Lee, C. W, I. 2008, A&A, 487, 993
Liseau, R., Goldsmith, P. F., Larsson, B., et al. 2012, A&A, 541, A73
Long, F., Herczeg, G. J., Pascucci, I., et al. 2017, ApJ, 844, 99
Loomis, R. A., Öberg, K. I., Andrews, S. M., et al. 2018a, AJ, 155, 182
Loomis, R. A., Oberg, K. I., Andrews, S. M., et al. 2018b, VISIBLE: VISIbility Based Line Extraction, Astrophysics Source Code Library, ascl:1802.006
Loomis, R. A., Öberg, K. I., Andrews, S. M., et al. 2020, ApJ, 893, 101
Lovas, F. J. 1985, JPCRD, 14, 395
Luspay-Kuti, A., Mousis, O., Lunine, J. I., et al. 2018, SSRv, 214, 115
Luspay-Kuti, A., Mousis, O., Pauzat, F., et al. 2022, NatAs, 6, 724
Marechal, P., Viala, Y. P., & Pagani, L. 1997, A&A, 328, 617
McClure, M. K., Rocha, W. R. M., Pontoppidan, K. M., et al. 2023, NatAs, 7, 431
McGuire, B. A. 2022, ApJS, 259, 30
McMullin, J. P., Waters, B., Schiebel, D., Young, W., & Golap, K. 2007, in ASP Conf. Ser. 376, Astronomical Data Analysis Software and Systems XVI, ed. R. A. Shaw, F. Hill, & D. J. Bell (San Francisco, CA: ASP), 127
Miotello, A., Kamp, I., Birnstiel, T., Cleeves, L. I., & Kataoka, A. 2023, in ASP Conf. Ser. 534, Protostars and Planets VII, ed. S. Inutsuka et al. (San Francisco, CA: ASP), 501
Mizushima, M., & Yamamoto, S. 1991, JMoSp, 148, 447
Müller, H. S. P., Thorwirth, S., Roth, D. A., & Winnewisser, G. 2001, A&A, 370, L49
Öberg, K. I., Guzmán, V. V., Merchantz, C. J., et al. 2017, ApJ, 839, 43
Öberg, K. I., Linnartz, H., Visser, R., & van Dishoeck, E. F. 2009, ApJ, 693, 1209
Pickett, H. M., Poynter, R. L., Cohen, E. A., et al. 1998, JQSRT, 60, 883
Przybilla, N., Nieva, M.-F., & Butler, K. 2008, ApJL, 688, L103
Ripple, F., Heyer, M. H., Gutermuth, R., Snell, R. L., & Brunt, C. M. 2013, MNRAS, 431, 1296
Rubin, M., Altwegg, K., van Dishoeck, E. F., & Schwehm, G. 2015, ApJL, 815, L11
Rubin, M., Engrand, C., Snodgrass, C., et al. 2020, SSRv, 216, 102
Salinas, V. N., Hogerheijde, M. R., Mathews, G. S., et al. 2017, A&A, 606, A125
Schöier, F. L., van der Tak, F. F. S., van Dishoeck, E. F., & Black, J. H. 2005, A&A, 432, 369
Steinbach, W., & Gordy, W. 1975, PhRvA, 11, 729
Taquet, V., van Dishoeck, E. F., Swayne, M., et al. 2018, A&A, 618, A11
Teague, R. 2020, richteague/keplerian_mask: Initial Release v1.0, Zenodo, doi:10.5281/zenodo.4321137
Teague, R., Bae, J., Andrews, S. M., et al. 2022, ApJ, 936, 163
Teague, R., Bae, J., Huang, J., & Bergin, E. A. 2019, ApJL, 884, L56
van Dishoeck, E. F., Herbst, E., & Neufeld, D. A. 2013, ChRv, 113, 9043
van Dishoeck, E. F., Kristensen, L. E., Mottram, J. C., et al. 2021, A&A, 648, A24
van Dishoeck, E. F., Thi, W. F., & van Zadelhoff, G. J. 2003, A&A, 400, L1
Walsh, C., Loomis, R. A., Öberg, K. I., et al. 2016, ApJL, 823, L10
Walsh, C., Nomura, H., & van Dishoeck, E. 2015, A&A, 582, A88
Whittet, D. C. B. 2010, ApJ, 710, 1009
Wilson, T. L., & Rood, R. 1994, ARA&A, 32, 191
Yang, Y.-L., Green, J. D., Pontoppidan, K. M., et al. 2022, ApJL, 941, L13
Zhang, K., Pontoppidan, K. M., Salyk, C., & Blake, G. A. 2013, ApJ, 766, 82